


Disentangling polycationic fullerenes produced from glassy carbon with multireflection time-of-flight mass spectrometry

Paul Fischer^{✉*} and Lutz Schweikhard

Institut für Physik, Universität Greifswald, 17487 Greifswald, Germany

 (Received 26 September 2022; accepted 14 November 2022; published 14 December 2022)

Carbon-cluster ions are produced by laser irradiation of glassy carbon in high vacuum. In the case of positively charged species, a bimodal cluster distribution including fullerenes with cluster-size-to-charge ratios of up to a few hundred is observed. Resolving isotopologues by use of a multireflection time-of-flight mass spectrometer allows the detection and abundance determination of multiply charged clusters. It is found that mono-, di-, and tricationic fullerenes are produced, have similar size-over-charge-state ranges, and follow log-normal distributions known to be characteristic of an underlying coalescent growth. A statistical simulation is shown to reproduce the results.

DOI: [10.1103/PhysRevResearch.4.043187](https://doi.org/10.1103/PhysRevResearch.4.043187)

I. INTRODUCTION

Gas-phase atomic clusters, aggregates of a few to a few thousand atoms, have been produced by a variety of techniques [1,2]. Generally, a bulk material is vaporized via, e.g., ion sputtering, melting, or laser ablation, which yields neutral and ionized atoms and small clusters. The use of cooling/aggregation gas then enables the vaporized material to grow to large cluster sizes. Postionization by photons or electrons can be employed to increase the yield of charged particles and/or populate higher charge states.

One of the most versatile types of cluster sources was introduced by Smalley and co-workers, combining pulsed laser ablation with a supersonic jet expansion [3]: Clusters from any metal as well as carbon and silicon could be produced. In fact, the use of graphite as the target material led to the Nobel Prize-winning discovery of fullerenes and their most prominent representative, buckminsterfullerene C_{60} [4].

Laser-ablation sources without additional aggregation gas, in contrast, are commonly used to ionize samples of biomolecules embedded in crystalline matrix structures of organic compounds, enabling what is referred to as matrix-assisted laser desorption/ionization mass spectrometry (MALDI-MS) [5]. Although less common, high-vacuum laser-ablation sources are also utilized for direct cluster production from thin films or bulk targets without chemical preparation [6–10]. Due to the absence of cooling gas to facilitate cluster growth, however, the resulting cluster-size distribution is typically small and more dependent on the target material.

Carbon fullerenes show a different behavior, as reported by Maul *et al.* [11,12]. They performed laser ablation with a

337-nm nitrogen laser on glassy carbon [13] covered with a photoabsorber and observed cationic fullerene clusters with up to approximately 200 atoms. However, the authors explicitly mention that fullerenes were not observed from pure glassy carbon.

Here we also report the observation of large even-sized carbon-cluster cations with up to a few hundred atoms produced by laser ablation of glassy carbon at 532 nm. However, no photoabsorber or chemical preparation is employed. Furthermore, the use of high-resolution multireflection time-of-flight (MR-ToF) mass spectrometry allows the identification of fullerenes and the accurate determination of their size distribution. The present fullerene production might be related to the use of 532-nm laser light or the longer pulse duration compared to the studies of Maul *et al.* (approximately 10 ns versus approximately 4 ns). A significant difference of the resulting mass spectra is the presence of multiply charged fullerene species C_n^{2+} and C_n^{3+} .

II. EXPERIMENTAL SETUP

The setup (Fig. 1) combines a high-vacuum laser-ablation source with an MR-ToF analyzer capable of storing ions by capturing them between two electrostatic ion mirrors [14,15]. Ions are produced by pulsed laser irradiation (Litron TRLi DPSS 170-100, $\lambda = 532$ nm, 10 ns pulse width, 2 mm diameter on target) of target plates biased to ± 2 kV for the extraction of cations or anions. The ablated cloud of ions and neutrals is not cooled by additional aggregation gas.

Ions leave the source region with a total energy of 2 keV per charge state and are guided towards the analyzer by ion-optical lenses and deflectors. They are captured by lowering their energy between the electrostatic mirrors via an in-trap lift [16], the potential of which is switched from approximately 800 V to ground. After a storage time during which the captured species revolve between the mirrors, the exit-side mirror potential is switched off [17] to release them towards a channeltron detector with 5-kV conversion dynode (DeTech, 402AH). The amplified signals (Ortec, VT120A) are recorded

*Corresponding author: paul.fischer@uni-greifswald.de

Published by the American Physical Society under the terms of the [Creative Commons Attribution 4.0 International license](https://creativecommons.org/licenses/by/4.0/). Further distribution of this work must maintain attribution to the author(s) and the published article's title, journal citation, and DOI.

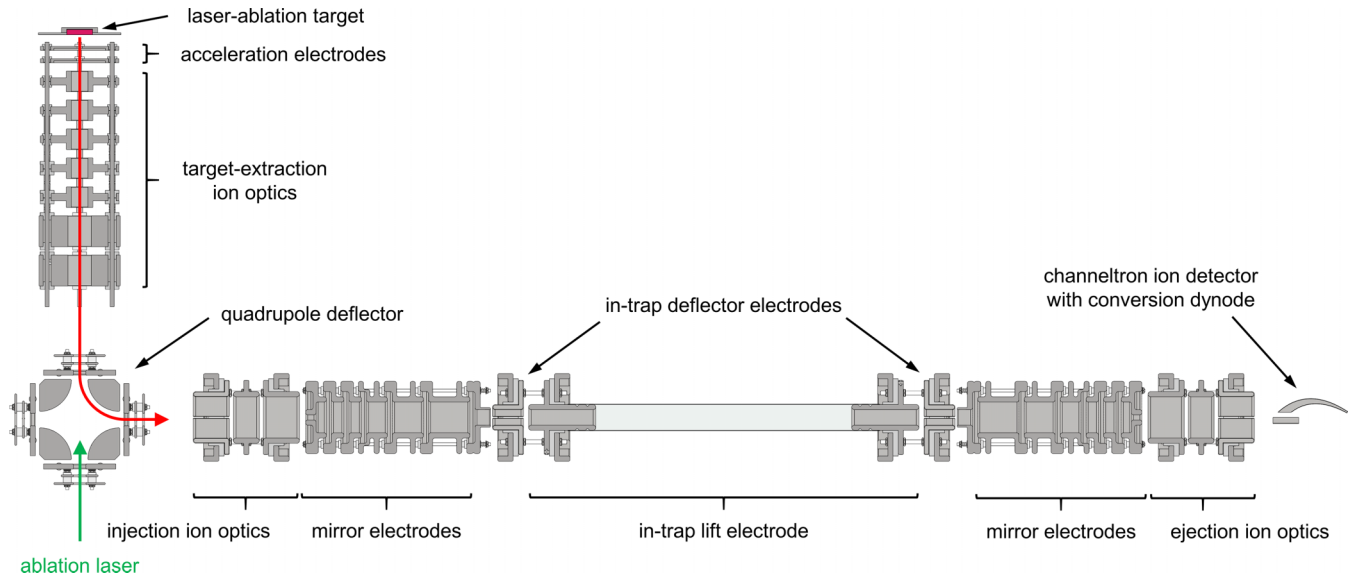


FIG. 1. Experimental setup including laser-ablation source and multireflection time-of-flight analyzer. The ion flight path is indicated in red.

by a multiscaler (Fast ComTec, MCS6A). During storage, ion species can be selectively retained in the analyzer by synchronized switching of in-trap deflector electrodes (see Fig. 1) [18,19].

III. RESULTS AND DISCUSSION

A. Single-path spectra of carbon-cluster cations and anions

Figure 2 shows an overview of all ions produced by laser ablation from a glassy carbon target (Sigradur G, HTW

Hochtemperatur-Werkstoffe GmbH) by forgoing ion capture to record linear time-of-flight spectra. The expected flight times of several n/z values are marked with vertical lines. While the small anionic clusters show a trend of odd-even staggering, the small cations have a smoother distribution. Notably, however, there are significantly larger clusters in the cationic spectrum: After a drop in production rate around $n/z = 20$, a second distribution ranging from $n/z \approx 40$ to $n/z \approx 600$ is detected which is reminiscent of previous fullerene studies [4,11,12].

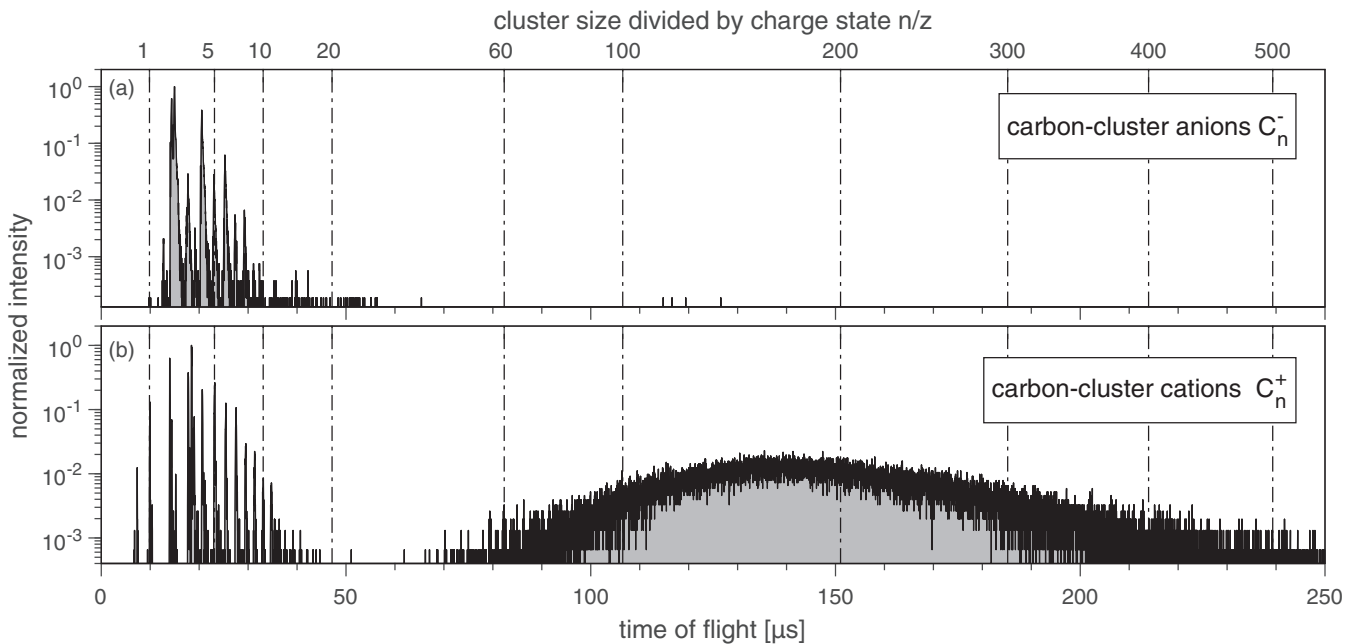


FIG. 2. Single-path time-of-flight spectra of carbon-cluster (a) anions and (b) cations produced by laser ablation of a Sigradur target. Selected cluster sizes are marked by vertical lines. The anion (cation) spectrum is recorded with 4.2 mJ (2.3 mJ) ablation-laser pulse energy, which is chosen to produce sufficiently high count rates without saturating the ion detector.

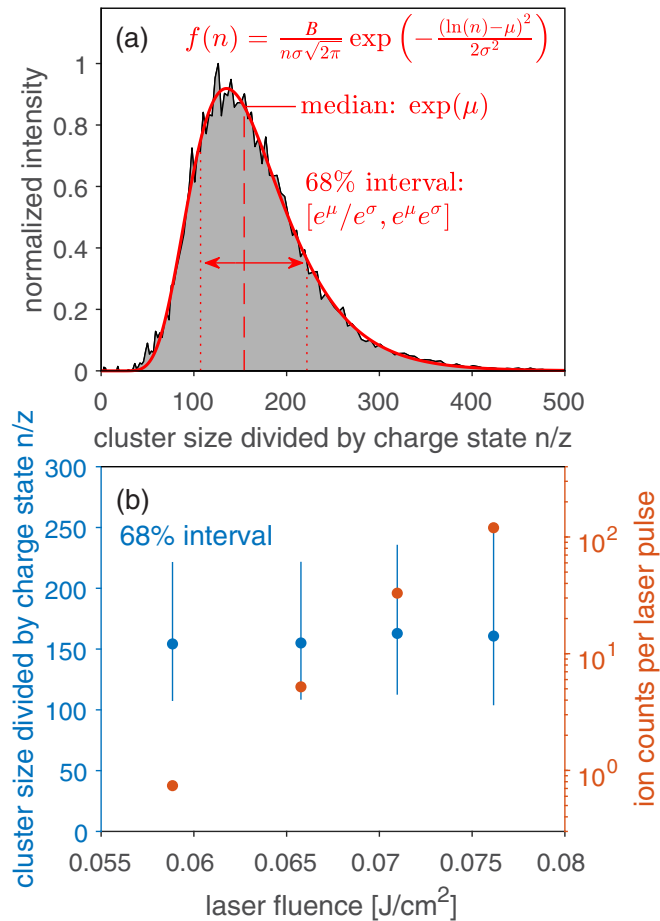


FIG. 3. (a) Abundance spectrum of cationic clusters from Fig. 2 with log-normal distribution fitted to the data (red line). (b) Median $\exp(\mu)$ (blue dots) and 68% interval $[\exp(\mu)/\exp(\sigma), \exp(\mu)\exp(\sigma)]$ (blue lines) of n/z as a function of ablation-laser fluence as well as ion counts per laser pulse (orange dots).

B. Description of the high-mass cluster distribution

It is apparent from Fig. 2 that the envelope of large clusters is asymmetric. This becomes even more obvious when the TOF data is transformed into a mass spectrum [Fig. 3(a)]. In fact, the spectrum is well described by a log-normal distribution

$$f(n|B, \sigma, \mu) = \frac{B}{n\sigma\sqrt{2\pi}} \exp\left(-\frac{[\ln(n)-\mu]^2}{2\sigma^2}\right) \quad (1)$$

[red solid line in Fig. 3(a)] with scaling parameter B , shape parameter σ , and median $\exp(\mu)$ [20].

Varying the ablation-laser pulse energy does not significantly affect the observed spectrum (Fig. 3). Note that, while the laser fluence is only varied across a moderate region, the detected ion counts per pulse span two orders of magnitude [right axis in Fig. 3(b)]. Lower pulse energies lead to the loss of the ion signal, while higher ones saturate the detector.

Arising from the principle of multiplicative processes [20], the log-normal distribution has been shown to describe cluster formation by coalescent growth [21], that is, a process based on reactant clusters of size n_i and n_j forming a cluster of size $n_i + n_j$. More precisely, the log-normal distribution is found

as the asymptotic solution to the Smoluchowski coagulation equation [22] — which models the concentration of particle species as they coalesce — for large cluster sizes and long reaction times compared to the inverse of the interaction rate. A more detailed description of the Smoluchowski equation and the coalescent growth process is given in Sec. IV.

We note that a decrease in efficiency of the channeltron detector towards the higher masses is likely to affect the observed distribution. However, since such a decrease should be smooth and since the envelope of the observed ion signal is well described by a log-normal function, we still expect the measured distribution to be representative.

C. Confirmation of fullerenes and discovery of higher charge states

The observation of large-size carbon clusters suggests the presence of fullerenes. It has been reported that commercial glassy carbons exhibit fullerene-related structures due to the pyrolysis process through which they are created [23,24], explaining some of their desirable properties such as gas and liquid impermeability, resistance to chemical attack, and high thermal stability [25].

Fullerene structures can only be formed with an even number of atoms [2]. In line with this principle, the spectra of Maul *et al.* show no signals at odd cluster sizes (see Figs. 1 and 3 in Refs. [11,12], respectively). This confirms the clusters are indeed fullerenes and also excludes the presence of doubly charged species. Doubly charged clusters with $2n$ carbon atoms would yield signals at each integer value n . Indeed, Maul *et al.* do not mention fullerenes with $z > 1$.

In contrast, ion signals are visible at odd n/z values in the present case when utilizing the multireflection capabilities of the setup to reach higher mass resolving powers: Fig. 4 shows the cluster distribution after three revolutions in the MR-ToF analyzer. The increased mass resolving power reveals smaller signals between the $2n$ comb expected for fullerenes (see the inset in Fig. 4). In the framework of the fullerene hypothesis, these signals suggest the presence of doubly charged cluster ions. There is, however, no conclusive evidence from Fig. 4, as nonfullerene carbon clusters could be present.

Increasing the number of revolutions N in the MR-ToF analyzer yields yet higher mass resolving powers, as is illustrated in Fig. 5 by N -versus-ToF plots: The storage time is increased in steps matching integer multiples of the revolution period $T \approx 116.15 \mu\text{s}$ of the reference C_{100}^+ . The start of the ToF recording is synchronized to the ejection from the analyzer and spectra are plotted as a two-dimensional map with the vertical axis indicating the revolution number.

The reference species is observed at the same flight time in each spectrum, leading to a straight vertical line. Figure 5(b) shows neighboring cluster sizes separating with higher revolution numbers. Note that lapping species are ejected by the transversal MR-ToF deflectors [18]. Thus, all species observed in a given spectrum are recorded at identical lap numbers. After about $N \approx 50$ revolutions, only a single cluster size remains in the analyzer. For $N \gtrsim 100$ the isotopologues, i.e., clusters of identical size with different isotopic compositions $^{12}\text{C}_{n-k} \text{ } ^{13}\text{C}_k$, $k = 0, 1, 2, \dots$, are resolved.

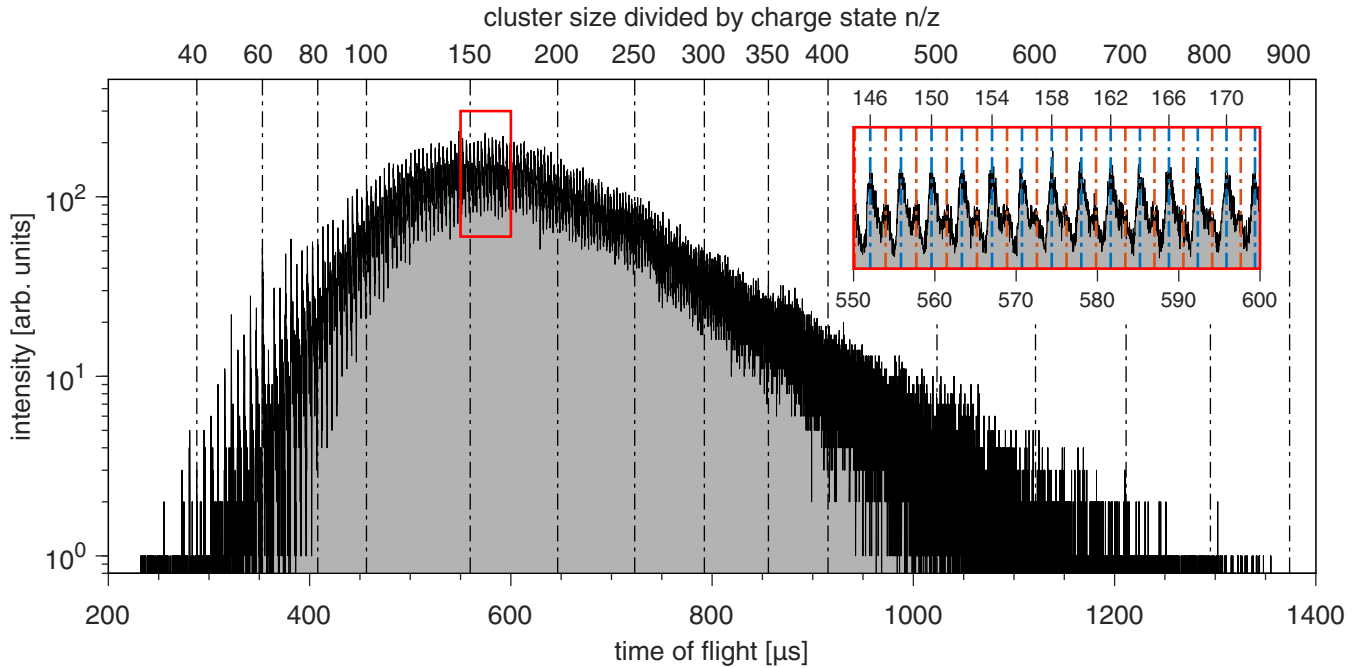


FIG. 4. Time-of-flight spectrum of cluster distribution after three revolutions in the MR-ToF analyzer. Nine ToF ranges are recorded separately to cover the full size range. The inset shows the part of the spectrum marked by the red rectangle. Even cluster sizes are marked with blue and odd cluster sizes (suggesting dicationic species) with orange lines in the inset.

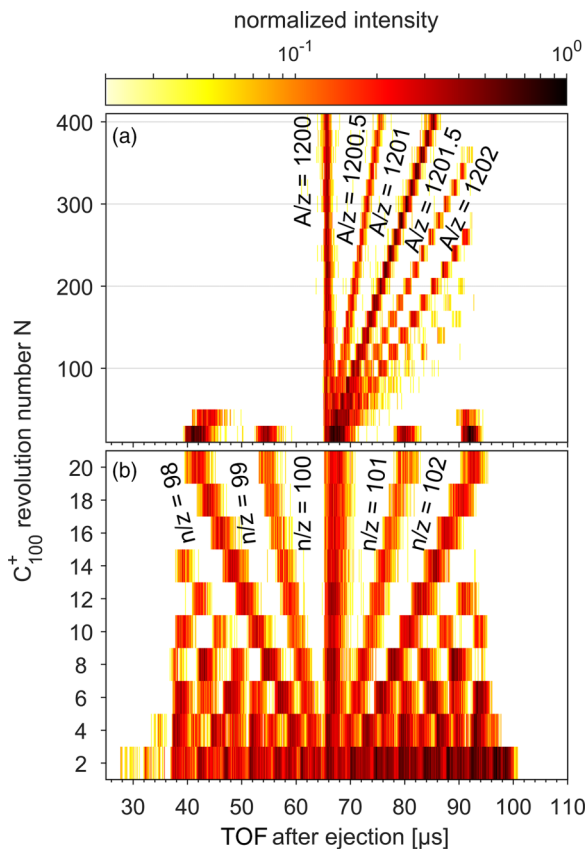


FIG. 5. N -versus-ToF plot of cluster species around $n/z = 100$ for (b) low and (a) higher revolution numbers.

Figure 6 shows the region around cluster size $n/z = 100$ after 200 revolutions. Notably, half-integer mass-number-to-charge ratios A/z are found to correspond to some of the signals, which is conclusive proof of the presence of doubly charged species. In addition, signals with third-integer spacing are found, providing evidence of trications. No higher charge states are observed.

The isotopologue-abundance distribution is characteristic of a cluster’s size n but independent of its charge state. The ^{12}C and ^{13}C isotopes constitute 98.9% and 1.1% of natural carbon, respectively [26]. Figure 6 includes the relative intensities for $n = 101$ and 202 clusters expected from the corresponding binomial distributions and normalized to the highest measured ToF signal (crosses and circles, respectively). Obviously, this provides further confirmation that the signals from $n/z = 1212$ to 1216 result from dications. Since they are fully explained by the abundances of the C_{202}^{2+} isotopologues, it follows that no signals are observed from odd-sized clusters like C_{101}^+ which would not obey the even-number rule. Thus, it can be concluded that indeed only fullerenes contribute to this spectrum. The signals starting from $A/z = 1200$, on the other hand, are a mixture of C_{100}^+ and C_{200}^{2+} isotopologues. Note that their signals at whole mass numbers cannot be resolved as the corresponding mass-over-charge values differ only by their molecular binding energies.

D. Abundances as a function of charge state

While the log-normal distribution in the n/z spectrum of Fig. 3(a) is composed of a mix of C_n^+ , C_n^{2+} , and C_n^{3+} clusters, Fig. 6 suggests a considerable part of the unresolved fullerene spectrum to be composed of dications. Figure 7 shows the envelopes for the individual charge

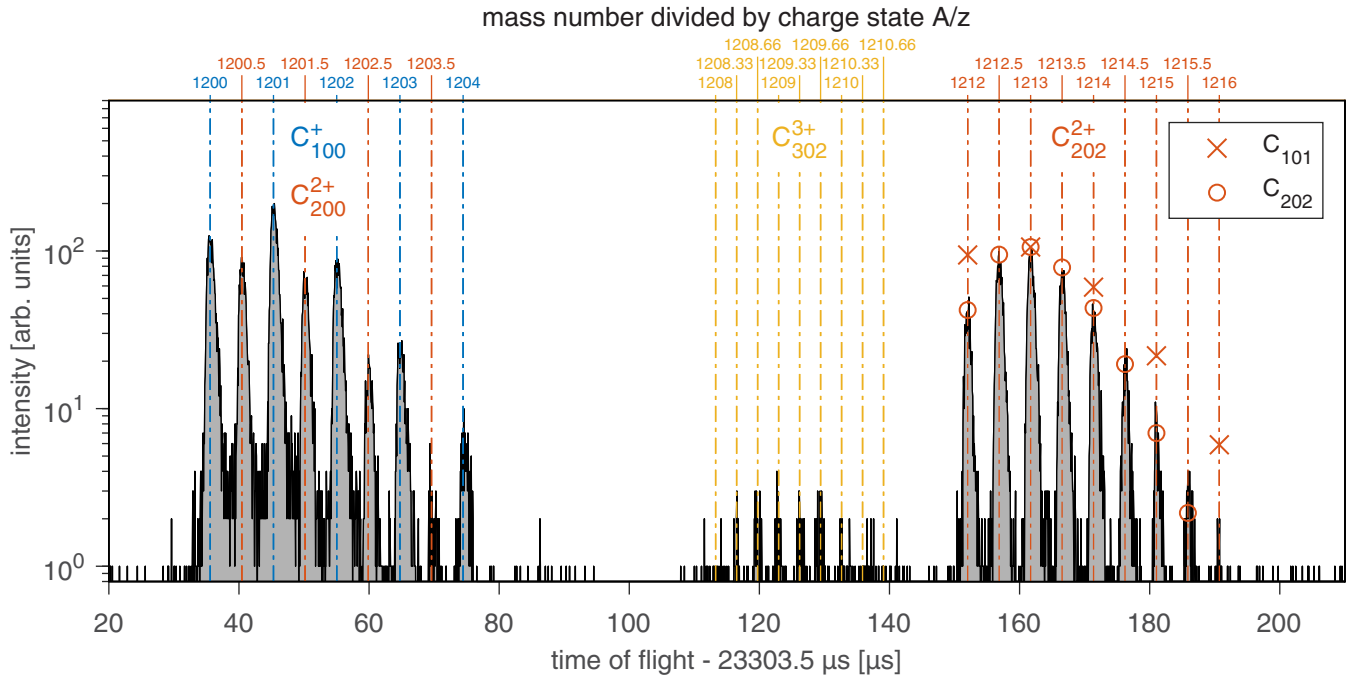


FIG. 6. Time-of-flight spectrum of cluster species around $n/z = 100$ after 200 revolutions with resolved isotopologues. Signals resulting from mono-, di-, and tricationic species are marked by blue, orange, and yellow lines, respectively. Crosses and circles show calculated isotopologue distributions for C_{101} and C_{202} clusters, respectively.

states as obtained from selected cluster sizes with their absolute production rates plotted over n/z [Fig. 7(a)] and their rates normalized to their maxima plotted over n [Fig. 7(b)]. Log-normal distributions are fitted to all three data sets (solid lines). Their medians are found at $(n/z)_{\text{med}} = 185(15)$, $150(5)$, and $250(20)$, i.e., $n_{\text{med}} = 185(15)$, $300(10)$, and $750(60)$ for singly, doubly, and triply charged clusters, respectively. Thus, the average cluster size increases by factors roughly equal to the ratio of the respective charge states.

In Fig. 8, the results of detailed abundance measurements are shown for the onset region of the polycations. Their appearance sizes depend on the experimental conditions. In the present study, they are $n \approx 40, 90$, and 260 for $z = 1, 2$, and 3 , respectively.

IV. MODELING CLUSTER GROWTH

The production of clusters by coalescence from smaller pieces has already been treated extensively in the literature [21,27,28]. In particular, it is well known that a resulting log-normal size distribution is indicative of this process, where reactant clusters form larger clusters through near-inelastic two-body collisions. Fusion reactions of laser-ablated C_{60} clusters from thin films have been studied [29]. More specifically, Maul *et al.* have used coalescence to explain their findings about the production of fullerenes by laser ablation [11,12]. However, charge-state considerations have not yet been included.

A coalescing cluster ensemble can be modeled by a set of Smoluchowski coagulation equations

$$\frac{dc_i}{dt} = \frac{1}{2} \sum_{n_j=1}^{n_i-1} K(n_j, n_{i-j}) c_j c_{i-j} - c_i \sum_{n_j=1}^{\infty} K(n_i, n_j) c_j \quad (2)$$

which describe the change in concentration c_i of a cluster species of size n_i [22]. The first term in (2) comprises the coalescence of smaller species $n_i - n_j$ and n_j to increase the concentration of n_i and the second the formation of larger species, reducing the concentration of n_i . The rate kernels $K(n_i, n_j)$ act as size-dependent scaling factors for the growth process. Many kernels derived from physical arguments are homogeneous (see, e.g., Table 1 in [28]), i.e., they satisfy

$$K(\alpha n_i, \alpha n_j) = \alpha^\lambda K(n_i, n_j) \quad (3)$$

for some exponent λ (the degree of homogeneity).

Exact solutions for (2) exist only for a few particular kernels [28]. An alternative approach uses a statistical treatment of the cluster ensemble. As a first step toward a qualitative understanding of the present data, such a treatment, closely related to the work of Marcus [30] and Lushnikov [31], is applied. It has been extended by introducing the possibility of several charge states. The starting point is an unordered set $\{(n_1, z_1), \dots, (n_m, z_m)\}$ of a finite number of particles with sizes n_1, \dots, n_m and charge states z_1, \dots, z_m . The following algorithm is applied.

(1) Randomly select two particles k and l ($k \neq l$) from the set.

(2) Create a uniform random number $0 \leq r_1 \leq 1$. If $r_1 > P(n_k, n_l)$ go to step 1.

(3) If $z_k z_l \neq 0$, create a uniform random number $0 \leq r_2 \leq 1$. If $r_2 > Q(z_k, z_l)$ go to step 1.

(4) Delete (n_k, z_k) and (n_l, z_l) , add $(n_k + n_l, z_k + z_l)$ to the set, and go to step 1.

The probabilities $P(n_k, n_l)$ are closely related to the Smoluchowski rate kernels. They are symmetric by construction of the algorithm, that is, the reaction $(n_k, z_k) + (n_l, z_l) \rightarrow (n_k + n_l, z_k + z_l)$ remains for the switching of k and l . Following the

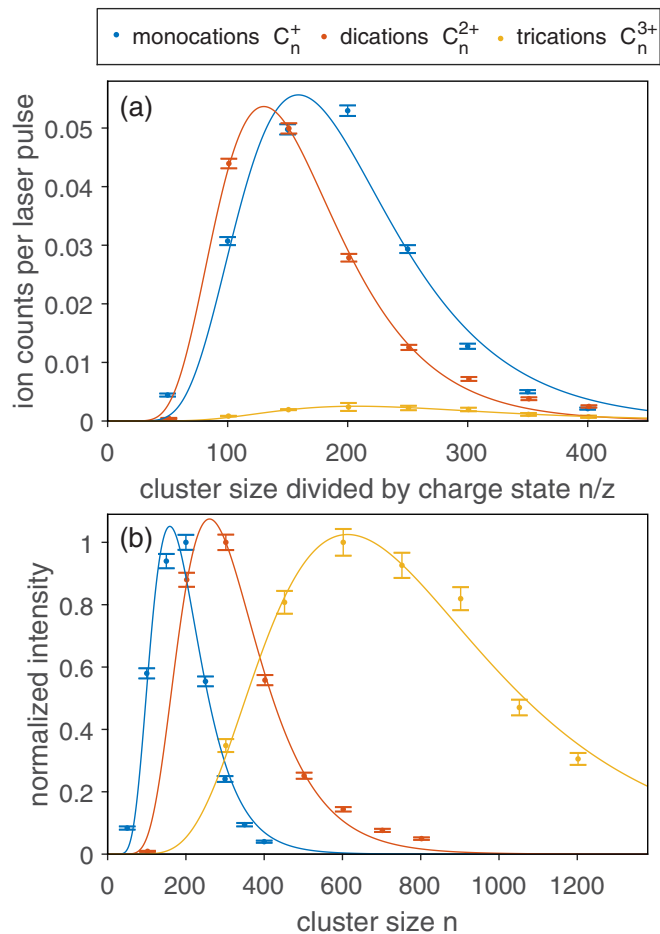


FIG. 7. (a) Production rates of selected mono-, di-, and tricationic carbon clusters. (b) Same data as in (a) normalized to each distribution’s maximum and plotted over proper cluster size. Log-normal distributions are fitted to all data sets (solid lines).

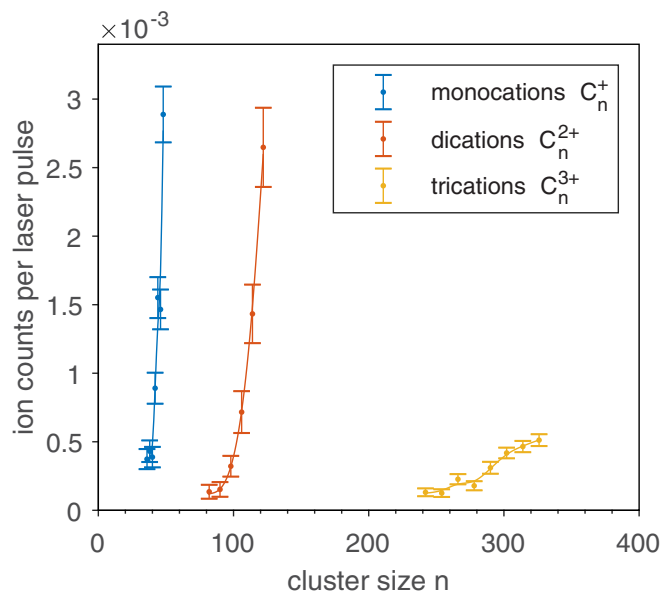


FIG. 8. Production rates of smallest observed mono-, di-, and trications for the present experimental conditions. Data sets have been interpolated with splines (solid lines) to guide the eye.

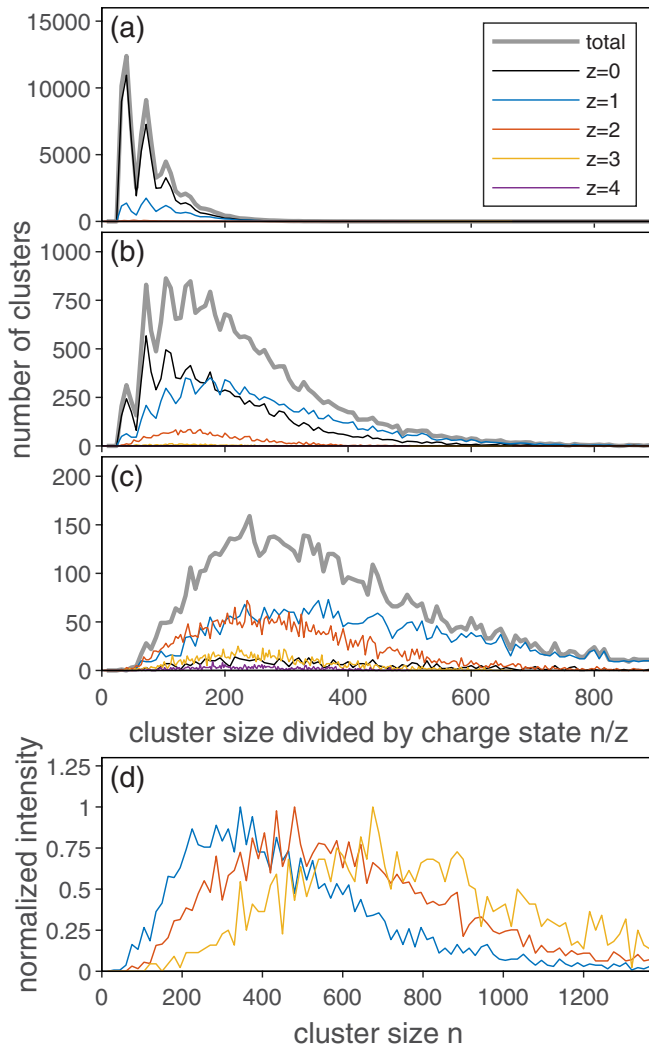


FIG. 9. Evolution of simulated fullerene ensemble following the algorithm outlined in the text. Charge-state-resolved distributions after (a) 20×10^6 , (b) 40×10^6 , and (c) 60×10^6 iterations are plotted over n/z . (d) Distributions of $z = 1, 2$, and 3 after 60×10^6 iterations from (c) normalized to their maxima and plotted over proper cluster size n .

literature, homogeneous probabilities with power-law scaling

$$P(n_k, n_l) = P(1, 1)(n_k n_l)^{\lambda/2} \tag{4}$$

are used here, allowing the calculation of all values from a given $P(1, 1)$ and scaling exponent λ [32]. To yield the sloped cluster-size distributions observed, λ must be negative, reflecting that larger clusters are slower than smaller ones at a given temperature and therefore their collision rates are lower [21].

Step 3 of the algorithm is introduced to account for the total coalescence probability’s dependence on the reactants’ charge states. To include the effect of the Coulomb repulsion between two charged species, the probability is decreased by

$$Q(z_k, z_l) = \frac{C}{z_k z_l} \tag{5}$$

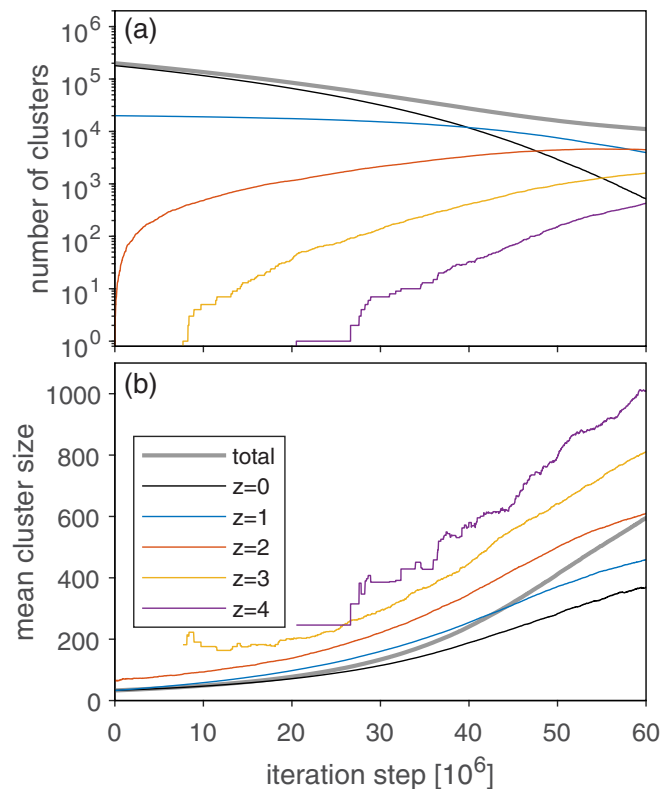


FIG. 10. (a) Total number of clusters (regardless of size) with charge states $z = 0$ through $z = 4$ as well as total cluster number (gray line) over number of iteration steps. (b) Arithmetic mean of all cluster sizes exhibiting a given charge state in each iteration step as well as mean size of the full set (gray line).

with a scaling constant $0 < C \leq 1$ if both z_k and z_l are nonzero. Note that only positive charges are considered. Successful fusion reduces the number of particles of the ensemble by one while conserving the number of atoms and charges.

Simulation parameters $P(1, 1) = 0.1$, $\lambda = -0.75$, and $C = 0.55$ as well as an initial ensemble of 200 000 particles of even-size clusters between $n = 24$ and 40 (90% neutral and 10% singly charged) result in the distributions shown in Fig. 9 after 20×10^6 , 40×10^6 , and 60×10^6 iterations of the algorithm. Increasing this number changes the results only marginally. Varying the scaling values affects the final size range and distribution of charge states. However, a full evaluation of the simulation approach and its parameters is beyond the scope of the present study.

The envelope of all clusters (gray line), i.e., all size and charge-state combinations, quickly follows a log-normal function, as do the distributions of the individual charge states. Oscillations due to the finite starting set are still visible after 20×10^6 and 40×10^6 iterations but are washed out as the

number of iterations is increased. Figures 9(c) and 9(d) show the final distributions plotted over n/z and n , respectively, in analogy to the experimental results in Fig. 7. The simulated set has grown to larger cluster sizes. This may be due to the negligence of decay mechanisms, such as dimer emission or break-off of larger fragments, in the present model. In addition, cluster-polarization effects may lead to further size dependences during the growth processes. Thus, the present modeling is in general not to be taken as a quantitative evaluation; after all, the parameter values found have no further physical motivation. Nonetheless, the simulation results resemble the experimental data, in particular concerning the fact that similar n/z ranges are populated for all observed charge states.

Tracking the number of all clusters and arithmetic mean of the size distributions for the charge states reveals this to be a persistent quality of the ensemble (Fig. 10): While the numbers of neutrals and monocations decrease, the higher charge states continuously increase. The mean sizes, which are representative of the populated size range, retain almost constant ratios to one another with the z values acting as scaling factors.

V. SUMMARY AND CONCLUSIONS

Large-size cationic carbon clusters are observed after laser ablation of glassy carbon without aggregation gas. The species are confirmed to be fullerenes by high-resolution multireflection time-of-flight mass spectrometry. Di- and trications are found within the fullerene ensemble, the distributions of which cover similar n/z ranges.

With confirmation by a statistical simulation, the results are interpreted as follows: It is known that fullerene-like structures are present in glassy carbon. Small fullerenes form as the bulk material is ablated by the laser pulse. Coalescent cluster growth is the prevalent mechanism forming larger clusters in the ablation plume, resulting in a log-normal size distribution. Other mechanisms, e.g., continuous pickup of atoms or the breakdown of large particles, would be expected to yield different abundance spectra. Di- and trications are formed by coalescence reactions of pairs of charged clusters during the evolution of the ensemble. If the fullerenes were to grow as mainly monocations (or neutrals) and the higher charge states were a product of subsequent photoionization, distributions over similar n , not similar n/z , ranges would be expected.

In contrast to the cations, no large anionic carbon clusters are observed. This is in agreement with the picture of coalescing fullerenes because the heat of condensation and the heating by the inelastic collision energy lead to electron emission rather than a loss of neutral carbon dimers in the case of excess electrons [33]. Thus, already the small anionic fullerenes, if formed at all, would be neutralized upon collision and lost from the spectrum.

[1] R. L. Johnston, *Atomic and Molecular Clusters* (Taylor & Francis, London, 2002).

[2] J. A. Alonso, *Structure and Properties of Atomic Nanoclusters*, 2nd ed. (Imperial College Press, London, 2011).

- [3] T. G. Dietz, M. A. Duncan, D. E. Powers, and R. E. Smalley, Laser production of supersonic metal cluster beams, *J. Chem. Phys.* **74**, 6511 (1981).
- [4] H. W. Kroto, J. R. Heath, S. C. O'Brien, R. F. Curl, and R. E. Smalley, C_{60} : Buckminsterfullerene, *Nature (London)* **318**, 162 (1985).
- [5] C. Jurinke, P. Oeth, and D. van den Boom, MALDI-TOF mass spectrometry, *Mol. Biotechnol.* **26**, 147 (2004).
- [6] R. L. Hettich, Structural investigations of aluminum cluster ions, Al_n^- ($n = 3-50$), *J. Am. Chem. Soc.* **111**, 8582 (1989).
- [7] A. Drescher, J. Kitching, J. E. Crawford, J. K. P. Lee, and G. Thekkadath, Studies of Sb and Bi cluster produced by laser desorption, *Z. Phys. D* **19**, 203 (1991).
- [8] H. S. Kim, T. D. Wood, A. G. Marshall, and J. Lee, Production of gold cluster ions by laser desorption/ionization Fourier-transform ion cyclotron resonance mass spectrometry, *Chem. Phys. Lett.* **224**, 589 (1994).
- [9] C. Stoermer, J. Friedrich, and M. M. Kappes, Observation of multiply charged cluster anions upon pulsed UV laser ablation of metal surfaces under high vacuum, *Int. J. Mass Spectrom.* **206**, 63 (2001).
- [10] P. Fischer and L. Schweikhard, Photofragmentation of $Bi_n^{+/-}$ clusters ($n = 2-19$) in an electrostatic ion beam trap, *Eur. Phys. J. D* **73**, 105 (2019).
- [11] J. Maul, T. Berg, E. Marosits, G. Schönhense, and G. Huber, Statistical mechanics of fullerene coalescence growth, *Phys. Rev. B* **74**, 161406(R) (2006).
- [12] J. Maul, Measurement of nanoparticle mass distributions by laser desorption/ionization time-of-flight mass spectrometry, *J. Phys.: Condens. Matter* **19**, 176216 (2007).
- [13] V. Uskoković, A historical review of glassy carbon: Synthesis, structure, properties and applications, *Carbon Trends* **5**, 100116 (2021).
- [14] D. Zajfman, O. Heber, L. Vejby-Christensen, I. Ben-Itzhak, M. Rappaport, R. Fishman, and M. Dahan, Electrostatic bottle for long-time storage of fast ion beams, *Phys. Rev. A* **55**, R1577 (1997).
- [15] W. H. Benner, A gated electrostatic ion trap to repetitiously measure the charge and m/z of large electrospray ions, *Anal. Chem.* **69**, 4162 (1997).
- [16] R. N. Wolf, G. Marx, M. Rosenbusch, and L. Schweikhard, Static-mirror ion capture and time focusing for electrostatic ion-beam traps and multi-reflection time-of-flight mass analyzers by use of an in-trap potential lift, *Int. J. Mass Spectrom.* **313**, 8 (2012).
- [17] S. Knauer, P. Fischer, G. Marx, B. Schabinger, L. Schweikhard, and R. N. Wolf, Multi-reflection time-of-flight mass spectrometry with combined in-trap lift capture and mirror-switch ejection, *Int. J. Mass Spectrom.* **423**, 46 (2017).
- [18] P. Fischer, S. Knauer, G. Marx, and L. Schweikhard, In-depth study of in-trap high-resolution mass separation by transversal ion ejection from a multi-reflection time-of-flight device, *Rev. Sci. Instrum.* **89**, 015114 (2018).
- [19] P. Fischer, G. Marx, and L. Schweikhard, Multiple ion capture and separation in an electrostatic storage device, *Int. J. Mass Spectrom.* **435**, 305 (2019).
- [20] J. Aitchison and J. A. C. Brown, *The Lognormal Distribution* (Cambridge University Press, Cambridge, 1957).
- [21] M. Villarica, M. J. Casey, J. Goodisman, and J. Chaiken, Application of fractals and kinetic equations to cluster formation, *J. Chem. Phys.* **98**, 4610 (1993).
- [22] M. V. Smoluchowski, Drei Vorträge über Diffusion, Brownsche Bewegung und Koagulation von Kolloidteilchen, *Z. Phys.* **17**, 557 (1916).
- [23] P. J. F. Harris, Fullerene-related structure of commercial glassy carbons, *Philos. Mag.* **84**, 3159 (2004).
- [24] S. Sharma, C. N. Shyam Kumar, J. G. Korvink, and C. Kübel, Evolution of glassy carbon microstructure: *In situ* transmission electron microscopy of the pyrolysis process, *Sci. Rep.* **8**, 16282 (2018).
- [25] G. M. Jenkins and K. Kawamura, *Polymeric Carbons: Carbon Fibre, Glass and Char* (Cambridge University Press, Cambridge, 1976).
- [26] J. Meija, T. B. Coplen, M. Berglund, W. A. Brand, P. D. Bièvre, M. Gröning, N. E. Holden, J. Irrgeher, R. D. Loss, T. Walczyk, and T. Prohaska, Isotopic compositions of the elements 2013 (IUPAC technical report), *Pure Appl. Chem.* **88**, 293 (2016).
- [27] R. Drake, in *Topics in Current Aerosol Research*, edited by G. M. Hidy and J. R. Brock (Pergamon, Oxford, 1972), Pt. 2, pp. 203–376.
- [28] D. J. Aldous, Deterministic and stochastic models for coalescence (aggregation and coagulation): A review of the mean-field theory for probabilists, *Bernoulli* **5**, 3 (1999).
- [29] R. Mitzner, B. Winter, C. Kusch, E. E. B. Campbell, and I. V. Hertel, Coalescence reactions in laser-induced fullerene desorption: The role of fragments, *Z. Phys. D* **37**, 89 (1996).
- [30] A. H. Marcus, Stochastic coalescence, *Technometrics* **10**, 133 (1968).
- [31] A. A. Lushnikov, Coagulation in finite systems, *J. Colloid Interface Sci.* **65**, 276 (1978).
- [32] J. Chaiken and J. Goodisman, Application of fractals and kinetic equations in modeling cluster and ultrafine particle size distributions, *Nanostruct. Mater.* **5**, 225 (1995).
- [33] N. Walsh, A. Lassesson, F. Martinez, G. Marx, and L. Schweikhard, Comparison of the low-energy decay mechanisms of C_{70}^+ and C_{70}^- , *Vacuum* **83**, 761 (2008).